# Truncated Fractional-Order Total Variation Model for Image Restoration

**Raymond Honfu Chan**[1] · **Hai-Xia Liang**[2] (ID)

## Abstract

Fractional-order derivative is attracting more and more interest from researchers working on image processing because it helps to preserve more texture than total variation when noise is removed. In the existing works, the Grunwald–Letnikov fractional-order derivative is usually used, where the Dirichlet homogeneous boundary condition can only be considered and therefore the full lower triangular Toeplitz matrix is generated as the discrete partial fractional-order derivative operator. In this paper, a modified truncation is considered in generating the discrete fractional-order partial derivative operator and a truncated fractional-order total variation (tFoTV) model is proposed for image restoration. Hopefully, first any boundary condition can be used in the numerical experiments. Second, the accuracy of the reconstructed images by the tFoTV model can be improved. The alternating directional method of multiplier is applied to solve the tFoTV model. Its convergence is also analyzed briefly. In the numerical experiments, we apply the tFoTV model to recover images that are corrupted by blur and noise. The numerical results show that the tFoTV model provides better reconstruction in peak signal-to-noise ratio (PSNR) than the full fractional-order variation and total variation models. From the numerical results, we can also see that the tFoTV model is comparable with the total generalized variation (TGV) model in accuracy. In

✉ Hai-Xia Liang
haixia.liang@xjtlu.edu.cn

Raymond Honfu Chan
rchan.sci@cityu.edu.hk

1 College of Science, City University of Hong Kong, Hong Kong, China

2 Department of Mathematical Sciences, Xi'an Jiaotong-Liverpool University, Suzhou 215123, Jiangsu, China

⌀ Springer

addition, we can roughly fix a fractional order according to the structure of the image, and therefore, there is only one parameter left to determine in the tFoTV model, while there are always two parameters to be fixed in TGV model.

## 1 Introduction

In 1992, Rudin et al. [1] first proposed the following minimization problem (the ROF model) for image noise removal:

$$\min_{u \in BV(\Omega)} \left\{ \lambda J(u) + \frac{1}{2} \|u - f\|_2^2 \right\}, \tag{1.1}$$

where $J(u) = \|\nabla u\|_1$, $\Omega \subset \mathbb{R}^2$ is an open and bounded domain, and $f \in L^2(\Omega)$ is the known noisy image. The deblurring problem can be modeled to solve the following adapted ROF minimization problem

$$\min_{u \in BV(\Omega)} \left\{ \lambda J(u) + \frac{1}{2} \|Au - f\|_2^2 \right\}, \tag{1.2}$$

where $A$ is a blurring operator and $f$ here is the known corrupted image by blur and noise. From then, the total variation (TV)-based regularization methods have been the absolutely leading methods for image restorations because of its good property in meanwhile preserving edges and removing noise. However, some texture structure is lost in the reconstruction process and the recovered image has a staircase effect, which is not hoped. Therefore, high-order total variation models are studied to deduce the staircase effect, for example, the Lysaker, Lundervold, Tai (LLT) model [2] named by the authors, the combined first- and second-order functional model [3,4] and the total generalized variation (TGV) model [5,6]. Recently, the fractional-order derivative category [7–9] begins to attract the interest from researchers in image processing. It also plays a role of higher- or lower-order derivative operator depending on the choice of the fractional order. The fractional-order variation regularizers have been studied in edge detection [10], image denoising problems [11–20], image deblurring [21], image segmentation [22], and image inpainting problem [23], etc. In all these papers, the fractional-order variation models have been shown to be efficient.

In this paper, we consider the following fractional-order variation-based minimization problem:

$$\min_{u} \left\{ \lambda J_\alpha(u) + \frac{1}{2} \|Au - f\|_2^2 \right\}, \tag{1.3}$$

where $J_\alpha(u) = \| |\nabla^\alpha u| \|_1$, $\nabla^\alpha u = (\nabla_x^\alpha u, \nabla_y^\alpha u)$ and $|\nabla^\alpha u| = \sqrt{(\nabla_x^\alpha u)^2 + (\nabla_y^\alpha u)^2}$. When the noise is removed, the fractional-order derivative can be treated as a high-pass filter. When $\alpha$ is larger, its high-pass capability is stronger. We need to choose an appropriate $\alpha$ to restrain the oscillatory components such that the texture can pass the filter. Therefore, we fix $\alpha \in [1, 2]$ as in [11,12,19,20]. The readers can consult [24] for more details on the high-pass property of the fractional-order derivative when $\alpha \in [1, 2]$. When $\alpha = 1$, (1.3) is actually the TV regularization model (1.2). In this paper, we first introduce a modified truncation to generate a truncated fractional-order derivative operator and then apply it to (1.4) to derive the following tFoTV model for image restoration

$$\min_u \left\{ \lambda J_\alpha^t(u) + \frac{1}{2}\|Au - f\|_2^2 \right\}. \tag{1.4}$$

Here $J_\alpha^t(u) = \| |\nabla^{\alpha,t} u| \|_1$, $\nabla^{\alpha,t} u = (\nabla_x^{\alpha,t} u, \nabla_y^{\alpha,t} u)$ denotes the truncated fractional-order gradient, which will be introduced in Sect. 2. Then, we apply the alternating direction method of multipliers (ADMM), pioneered by Glowinski and Marrocco [25], Gabay and Mercier [26], to solve the tFoTV model (1.4). In the numerical section, we first test the tFoTV, original full FoTV and the TV models on noise removal to show the efficiency of the truncation. Next, we test the tFoTV model, TV model and TGV model to restore the blurred image corrupted by Gaussian noise. The numerical results show that our tFoTV model produces more accurate reconstructions in peak signal-to-noise ratio (PSNR) than the TV model and it is comparable with the TGV model in accuracy. Particularly, the fractional order can be roughly fixed from the structure of the tested images, which make the implementation of ADMM for tFoTV model easier to tune than the TGV model.

The rest of the paper is organized as follows: In Sect. 2, we introduce the discrete fractional-order derivative, our modified truncation, and also give some notations. In Sect. 3, we mainly derive the ADMM algorithm and linearized ADMM for (1.4) under different boundary conditions. In Sect. 4, we provide a brief interpretation to the convergence. Section 5 shows the numerical comparison results. In Sect. 6, we give some conclusions.

## 2 Truncated Fractional-Order Derivative and Notations

We denote our images by two-dimensional matrix of size $n \times n$ with $i$ and $j$ denoting the column and the row pixel coordinates. $X$ is the Euclidean space $\mathbb{R}^{n \times n}$. As in [12,24], we use the definition of the Grunwald–Letnikov fractional-order derivative [8] in this paper. If $u \in X$, $\nabla^\alpha u$ is a vector in $Y = X \times X$. For the simplification, we give the main formula of the fractional derivative of $u \in \mathbb{R}^{n \times n}$ at $u_{i,j}$. The discrete fractional-order derivative at a pixel $(i, j)$ is defined as $(\nabla^\alpha u)_{i,j} = ((\nabla_x^\alpha u)_{i,j}, (\nabla_y^\alpha u)_{i,j})$, where

$$(\nabla_x^\alpha u)_{i,j} = \sum_{s=0}^{\infty} \omega_s^\alpha u_{i-s,j}, \qquad (\nabla_y^\alpha u)_{i,j} = \sum_{s=0}^{\infty} \omega_s^\alpha u_{i,j-s}, \tag{2.1}$$

where the Dirichlet homogeneous boundary condition can only be considered. $\omega_s^\alpha$ is the real coefficient defined by

$$\omega_s^\alpha = (-1)^s \frac{\Gamma(\alpha+1)}{\Gamma(s+1)\Gamma(\alpha-s+1)} = \begin{cases} 1, & s = 0, \\ (-1)^s \frac{\alpha(\alpha-1)\cdots(\alpha-s+1)}{s!}, & s = 1, 2, \cdots. \end{cases} \quad (2.2)$$

The generalized binomial coefficients, defined in (2.2) in terms of the Gamma function, can be computed by the following recurrence relationships

$$\omega_0^\alpha = 1; \ \omega_s^\alpha = \omega_{s-1}^\alpha \cdot \left(1 - \frac{\alpha+1}{s}\right), \quad s = 1, 2, \cdots \quad (2.3)$$

and make the following equality hold:

$$\sum_{s=0}^{\infty} \omega_s^\alpha = 0.$$

Notice that when $\alpha = 1$ and $\alpha = 2$, $\omega_s^\alpha$ always equals zero when $s \geqslant 2$ and $s \geqslant 3$, respectively. When $\alpha \in (1, 2)$, the coefficients never vanishes. The partial fractional-order derivative operators $\nabla_x^\alpha$, $\nabla_y^\alpha$ can be obtained by the following Kronecker product:

$$\nabla_x^\alpha = I_n \otimes U^\alpha, \ \nabla_y^\alpha = U^\alpha \otimes I_n,$$

where $\otimes$ denotes the Kronecker product and $I_n$ is the $n$th-order identity matrix. If the Dirichlet homogeneous boundary condition is considered, the partial fractional-order derivative matrices $\nabla_x^\alpha$, $\nabla_y^\alpha$ are both matrices of block Toeplitz with Toeplitz blocks. $U^\alpha$ is an $n \times n$ Toeplitz lower triangular matrix whose first column is $(\omega_0^\alpha, \omega_1^\alpha, \cdots, \omega_{n-1}^\alpha)^\top$. When $\alpha \in (1, 2)$, the sum of any row of $U^\alpha$ will not equal zero. Therefore, two problems occur when the fractional-order derivative is used. One is that the fractional-order derivative of constant images never equals zero. Another one is that the fractional-order gradient operator based on the periodic boundary condition and Neumann boundary condition fails to be generated, since we have to compute infinitely many $\omega_s^\alpha$ and add them into $U^\alpha$. To solve these two problems, we propose the following truncation method to approximate the fractional-order derivative by using $K (2 \leqslant K \leqslant N$ for $1 < \alpha < 2)$ pixels. We first define

$$\begin{cases} \tilde{\omega}_s^\alpha = \omega_s^\alpha, & s = 0, 1, 2, \cdots, K-2, \\ \tilde{\omega}_{K-1}^\alpha = \sum_{K-1}^{\infty} \omega_s^\alpha, & \\ \tilde{\omega}_s^\alpha = 0, & s = K, K+1, \cdots. \end{cases} \quad (2.4)$$

If the Dirichlet boundary condition is considered, $U^{\alpha,t}$ is defined to be $n \times n$ Toeplitz lower triangular matrix whose first column is $(\tilde{\omega}_0^\alpha, \tilde{\omega}_1^\alpha, \cdots, \tilde{\omega}_{n-1}^\alpha)^\top$. The sum of the entries in the $K$th row to $n$th row of $U^{\alpha,t}$ equals zero. If periodic or Neumann boundary condition is considered, the sum of entries in all the rows of $U^{\alpha,t}$ equals zero. The truncated fractional-order partial derivative operators are generated, respectively, by

$$\nabla_x^{\alpha,t} = I_n \otimes U^{\alpha,t}, \ \nabla_y^{\alpha,t} = U^{\alpha,t} \otimes I_n.$$

After taking the modified truncation (2.4), hopefully, this kind of truncation can improve the reconstruction results of fractional-order variational models greatly, which will be verified in Sect. 5. To learn more about the truncated fractional-order derivative operator, we give the following two remarks.

*Remarks*

1. If $K = 2$ , then $\tilde{\omega}_0^\alpha = 1$, $\tilde{\omega}_1^\alpha = -1$, and $\tilde{\omega}_k^\alpha = 0, k = 2, 3, \cdots$. The truncated fractional-order derivative is actually the first-order derivative no matter what value $\alpha$ equals.
2. If $K = 3$, then $\tilde{\omega}_0^\alpha = 1$, $\tilde{\omega}_1^\alpha = -\alpha$, $\tilde{\omega}_2^\alpha = \alpha - 1$, and $\tilde{\omega}_k^\alpha = 0, k = 3, 4, \cdots$. The truncated fractional-order derivative operator $[1, -\alpha, \alpha - 1] = [1, -2, 1] + (2 - \alpha)[0, 1, -1]$, which can be treated as a linear combination of the first-order and second-order derivatives.

## 3 The Algorithms

In this section, we apply the ADMM-based method to solve the tFoTV model (1.4). First, we introduce an auxiliary variable and transform (1.4) to be an equivalent constrained problem

$$\min_{u,d} \left\{ \lambda \|\|d\|\|_1 + \tfrac{1}{2} \|Au - f\|_2^2 \right\}$$
$$\text{s.t.} \qquad d = \nabla^{\alpha,t} u. \tag{3.1}$$

We define the following Lagrangian functional

$$\mathcal{L}(u, d; p) = \lambda \left( \|\|d\|\|_1 + \langle p, d - \nabla^{\alpha,t} u \rangle + \frac{1}{2\eta} \|d - \nabla^{\alpha,t} u\|_2^2 \right) + \frac{1}{2} \|Au - f\|_2^2, \tag{3.2}$$

where $p$ is a Lagrangian multiplier and $|d| = \sqrt{d_x^2 + d_y^2}$. According to our tests, it is enough to take $\eta = 1$.

It is known that one of the saddle points of the augmented Lagrangian functional corresponds to the minimizers of the constrained minimization problem (3.1) [27–29]. The following algorithm is usually used to find the saddle points of the augmented Lagrangian functional (3.2), i.e., to solve the fractional-order minimization model (1.4).

**Algorithm 1**:

Step 1  Initialize $p^0 = 0$;
Step 2  For $k = 0, 1, 2, \cdots$:

    (a) Compute $(u^k, d^k)$ as an (approximate) minimizer of the augmented Lagrangian functional with the Lagrange multiplier $p^k$, i.e.,

$$(u^{k+1}, d^{k+1}) \approx \arg\min_{u,d} \mathcal{L}(u, d, p^k), \qquad (3.3)$$

    where $\mathcal{L}(u, d, p^k)$ is defined as in (3.2).
    (b) Update $p^{k+1} = p^k + \frac{1}{\eta}(d^{k+1} - \nabla^{\alpha,t} u^{k+1})$.

Since the variables in (3.3) are coupled together, it is very difficult to solve it exactly. Therefore, the alternating minimization approach is applied to find its approximate minimizers. In the following part, we separate problem (3.3) into two subproblems and give details on how to find the approximate minimizers by using the alternative minimization approach.

To find the approximate minimizer of (3.3), the following two subproblems will be solved sequentially once in each iteration.

– $u$-subproblem: Given $d$,

$$\min_u \left\{ \lambda \left( \||d|\|_1 + \langle p^k, d - \nabla^{\alpha,t} u \rangle + \frac{1}{2\eta} \|d - \nabla^{\alpha,t} u\|_2^2 \right) + \frac{1}{2} \|Au - f\|_2^2 \right\}; \quad (3.4)$$

– $d$-subproblem: Given $u$,

$$\min_d \left\{ \||d|\|_1 + \langle p^k, d - \nabla^{\alpha,t} u \rangle + \frac{1}{2\eta} \|d - \nabla^{\alpha,t} u\|_2^2 \right\}. \qquad (3.5)$$

Next, we will show that the above two subproblems either have explicit solutions or can be solved by inexpensive numerical solvers.

### 3.1 Solving the *u*-Subproblem

Notice that $u$-subproblem is quadratic in $u$. To get the solution of (3.4), we only need to take the derivative to the energy functional in $u$ and then solve the following linear system

$$\left( \frac{\lambda}{\eta}(\nabla^{\alpha,t})^\top \nabla^{\alpha,t} + A^\top A \right) u = A^\top f + \frac{\lambda}{\eta}(\nabla^{\alpha,t})^\top (d + \eta p^k). \qquad (3.6)$$

If periodic boundary condition is considered, (3.6) can be exactly solved directly by the fast Fourier transform (FFT). If Neumann or Dirichlet homogeneous boundary condition is considered, the FFT cannot be applied. Therefore, in these cases, the preconditioned ADMM (PADMM) [30] can be applied to solve (3.1). It means that we alternate to update $u^{s+1}$ by solving the following minimization problem

$$u^{s+1} = \arg\min_u \left\{ \mathcal{L}(u, d; p^k) + \frac{1}{2}\|u - u^s\|_S^2 \right\}, \tag{3.7}$$

where $\|u - u^s\|_S^2 = \langle u - u^s, S(u - u^s)\rangle$ and $S = \frac{1}{\delta}I - \frac{\lambda}{\eta}(\nabla^{\alpha,t})^\top\nabla^{\alpha,t} - A^\top A$ is positive definite with suitable choice of $\delta$. Actually, the PADMM is equivalent to a linearized ADMM (LADMM). It is said that (3.7) is equivalent to update $u^{s+1}$ by solving the following linearized minimization problem

$$\min_u \left\{ \lambda\langle p^k, -\nabla^{\alpha,t}u\rangle + \frac{\lambda}{\eta}\langle(\nabla^{\alpha,t})^\top(\nabla^{\alpha,t}u^s - d), u - u^s\rangle + \langle A^\top(Au^s - f), u - u^s\rangle \right.$$
$$\left. + \frac{1}{2\delta}\|u - u^s\|_2^2 \right\},$$

which is also quadratic in $u$ and has solution

$$u^{s+1} = u^s + \delta\left[\frac{\lambda}{\eta}(\nabla^{\alpha,t})^\top(d + \eta p^k - \nabla^{\alpha,t}u^s) + A^\top(f - Au^s)\right]. \tag{3.8}$$

### 3.2 Solving the *d*-Subproblem

Similar to the isotropic total variation in [31], $d = (d_x, d_y)$ in (3.5) has a closed-form solution given by

$$\begin{aligned}(d_x)_{i,j} &= \max(v_{i,j}^k - \eta, 0)\frac{(\nabla_x^{\alpha,t}u - \eta p_x^k)_{i,j}}{v_{i,j}^k}, \\ (d_y)_{i,j} &= \max(v_{i,j}^k - \eta, 0)\frac{(\nabla_y^{\alpha,t}u - \eta p_y^k)_{i,j}}{v_{i,j}^k},\end{aligned} \tag{3.9}$$

where $p^k = (p_x^k, p_y^k)$ and $v_{i,j}^k = \sqrt{(\nabla_x^{\alpha,t}u - \eta p_x^k)_{i,j}^2 + (\nabla_y^{\alpha,t}u - \eta p_y^k)_{i,j}^2}$ .

Combining the above results together, (3.3) is solved by the following alternating minimization approaches under different kinds of boundary conditions.

**Algorithm 1.1**: Alternating minimization approach for solving (3.3) under *periodic boundary condition*

Step 1 Initialize $u^{k+1,0} = u^k$, $d^{k+1,0} = d^k$;
Step 2 For $l = 0, 1, 2, \cdots, L - 1$:

(a) Update $u^{k+1,l+1}$ by solving (3.6), i.e., solving

$$\left(\frac{\lambda}{\eta}(\nabla^{\alpha,t})^\top\nabla^{\alpha,t} + A^\top A\right)u = A^\top f + \frac{\lambda}{\eta}(\nabla^{\alpha,t})^\top(d^{k+1,l} + \eta p^k)$$

using FFT.
(b) Update $d^{k+1,l+1}$ using (3.9) for $u = u^{k+1,l+1}$ ;
Step 3 $u^{k+1} = u^{k+1,L}$, $d^{k+1} = d^{k+1,L}$.

**Algorithm 1.2**: Alternating minimization approach for solving (3.3) under *Dirichlet homogeneous boundary condition or Neumann boundary condition*

Step 1  Initialize $u^{k+1,0} = u^k$, $d^{k+1,0} = d^k$;

Step 2  For $l = 0, 1, 2, \cdots, L-1$:

(a) Update $u^{k+1,l+1}$ by (3.8) from $u^{k+1,l}$, i.e.,

$$u^{k+1,l+1} = u^{k+1,l} + \delta\left[\frac{\lambda}{\eta}(\nabla^{\alpha,t})^\top(d^{k+1,l} + \eta p^k - \nabla^{\alpha,t}u^{k+1,l}) + A^\top(f - Au^{k+1,l})\right];$$

(b) Update $d^{k+1,l+1}$ using (3.9) for $u = u^{k+1,l+1}$ ;

Step 3  $u^{k+1} = u^{k+1,L}$, $d^{k+1} = d^{k+1,L}$.

Algorithm 1 with Algorithm 1.1 is so-called ADMM for solving (1.4) under periodic boundary condition. Algorithm 1 with Algorithm 1.2 is so-called LADMM for solving (1.4) under Dirichlet homogeneous or Neumann boundary condition.

## 4 Brief Convergence Analysis

Since the convergence properties of the ADMM and LADMM have been discussed in amount of papers [28,30,32,33], in this section, we briefly interpret the convergence of the proposed ADMM algorithm for solving the tFoTV model. The readers can consult [30] for the convergence of the LADMM.

We would like to illustrate the convergence of the proposed Algorithm 1 with Algorithm 1.1 under periodic boundary condition. Our truncation method makes the sum of all rows of $U^{\alpha,t}$ equal to zero when the periodic boundary condition is considered, so that the truncated fractional-order gradient operator has similar properties to the gradient. For example, the null space of the truncated fractional-order gradient operator is generated by all the constant images. In this paper, we only consider the case when the blur operator $A$ is given. Using the same notations to the paper [28], we define

- $R$ by $R(\nabla^{\alpha,t}u) = \||\nabla^{\alpha,t}u|\|$;
- $F$ by $F(Au) = \frac{1}{2}\|Au - f\|_2^2$;
- $E$ by $E(u) = \lambda\||\nabla^{\alpha,t}u|\| + \frac{1}{2}\|Au - f\|_2^2$.

In addition, the blur is essentially averaging. The following four assumptions as in [28] hold for $R$, $F$ and the truncated fractional-order gradient operator $\nabla^{\alpha,t}$.

- Assumption 1: $\text{null}(\nabla^{\alpha,t}) \cap \text{null}(A) = \{0\}$;
- Assumption 2: $\text{dom}(R \circ \nabla^{\alpha,t}) \cap \text{dom}(F \circ A) \neq \varnothing$;
- Assumption 3: $F(\cdot)$ is convex, proper, and coercive;
- Assumption 4: $F(\cdot)$ is continuous over $\text{dom}(F)$.

Therefore, Theorem 4.1 and Theorem 4.2 in [28] can be adapted to have the following two convergence theorems for our proposed algorithm under periodic boundary condition. And the proofs can be obtained immediately just by replacing the $\nabla$ there by $\nabla^{\alpha,t}$ here.

**Theorem 4.1** *Assume that $(u^*, d^*; p^*)$ is a saddle point of $\mathcal{L}(u, d; p)$. Suppose that the minimization problem* (3.3) *is exactly solved in each iteration, i.e., $L \to \infty$ in Algorithm 1.1. Then, the sequence $(u^k, d^k; p^k)$ generated by Algorithm 1 satisfies*

$$\begin{cases} \lim\limits_{k \to \infty} R(p^k) + F(Au^k) = R(p^*) + F(Au^*) = E(u^*), \\ \lim\limits_{k \to \infty} \|p^k - \nabla^{\alpha, t} u^k\|_2 = 0. \end{cases} \tag{3.1}$$

*Moreover,* (3.1) *indicates that $u^k$ is a minimizing sequence of $E(\cdot)$. If the minimizer of $E(\cdot)$ is unique, then $u^k \to u^*$.*

**Theorem 4.2** *Assume that $(u^*, d^*; p^*)$ is a saddle point of $\mathcal{L}(u, d; p)$. Suppose that the minimization problem* (3.3) *is roughly solved in each iteration, i.e., $L = 1$ in Algorithm 1.1. Then, the sequence $(u^k, d^k; p^k)$ generated by Algorithm 1 satisfies*

$$\begin{cases} \lim\limits_{k \to \infty} R(p^k) + F(Au^k) = R(p^*) + F(Au^*) = E(u^*), \\ \lim\limits_{k \to \infty} \|p^k - \nabla^{\alpha, t} u^k\|_2 = 0. \end{cases} \tag{3.2}$$

*Moreover,* (3.2) *indicates that $u^k$ is a minimizing sequence of $E(\cdot)$. If the minimizer of $E(\cdot)$ is unique, then $u^k \to u^*$.*

The readers can consult [28] for the proof of Theorem 4.1 and Theorem 4.2 there.

## 5 Numerical Results

In this section, we implement Algorithm 1 on denoising and deblurring, respectively, to show the efficiency of the proposed tFoTV model. The peak signal-to-noise ratio (PSNR) is used to measure the quality of the recovered images, which is defined by

$$\text{PSNR} := 10 \log_{10} \frac{255^2}{\frac{1}{n^2} \|\hat{u} - u^*\|_2^2} (\text{dB}),$$

where $\hat{u}$ and $u^*$ are the original and recovered images, respectively. All the numerical experiments are performed by MATLAB R2014a (8.3.0.532) on MacPro of version 10.9.5 with 2.2 GHz Intel Core i7 and 16GB memory.

We first take the noise removal, for example, to show the following three issues. First, when we generate the fractional-order derivative operator with modified truncation, the best choice for the number of pixels is $K = 3$ in most cases. Second, the tFoTV model usually produces the most accurate reconstructions in PSNR comparing with the original FoTV model and TV model. Third, the tFoTV model for image restoration can be implemented under any boundary conditions. Next, we apply the tFoTV model to restore the image corrupted by blur and noise simultaneously and compare it with the TV model and TGV model. In all the tables and figures shown in this section, we

abbreviate the Neumann, periodic and Dirichlet homogeneous boundary conditions by SB, PB and ZB, respectively.

## 5.1 Numerical Results on Noise Removal

We do noise removal experiments under Neumann, periodic and Dirichlet homogeneous boundary conditions on all the examples in Fig. 1. We consider the white Gaussian noise removal. The noise level is taken to be $\sigma = 15, 20$ and $25$ for all the images, respectively. Algorithm 1 is implemented under a list of $\lambda$, a list of $K$ and a list of $\alpha$s in the tFoTV model (1.4). When $K < n$, the fractional-order derivative operator is generated with modified truncation (2.4). $K = n$ stands for the original FoTV under the Dirichlet homogeneous boundary condition.

From Figs. 2 to 5, we plot the PSNR values versus $\alpha$s for $K = 3, 6, n$ under the Dirichlet homogeneous boundary condition and for $K = 3$ under the periodic and Neumann boundary conditions, respectively. From the PSNR curves for Dirichlet homogeneous boundary condition, we see that the tFoTV with $K = 3$ produces the most accurate reconstructions for all the images. The PSNR curve at $\alpha = 1$ corresponds to the result by the TV model. For more information, the PSNR values obtained by TV, original FoTV and tFoTV models are listed in Table 1. The highest PSNR values have been marked in bold there. From Figs. 2 to 5 and Table 1, we see that the tFoTV always produces the best reconstructions compared to the TV model and original FoTV model.

We focus on the PSNR curves for $K = 3$. Figures 2 to 5 tell us that for the cartoon images we should fix $\alpha$ close to 1, where 1.2 is a good choice, as shown in Figs. 2(1)–(5), 3(1)–(5), 4(1)–(5). If there are some textures in the images, but not so much, we can roughly fix the fractional order around 1.5, as shown in Figs. 2(6)–(10), 3(6)–(10), 4(6)–(10). We find that $\alpha = 1.5$ produces the highest PSNR values in most cases, and the difference of the PSNR values for the cases of $\alpha = 1.4$, $\alpha = 1.5$ and $\alpha = 1.6$ is less than 0.1dB. For the images that have a lot textures, we should fix $\alpha$ close to 2. For example, we can fix $\alpha = 1.8$, as shown in Figs. 2(11), (12), 3(11), (12), 4(11), (12). Yacht image can be divided into two parts, shown in Fig. 5. Yacht (part1) is a simple cartoon image, and Yacht (part2) is a texture image. From Figs. 5(a1) to (a3) and 5(b1)



(1) Medical image  (2) Peppers  (3) Splash  (4) Jetplane  (5) Man  (6) Baby

(7) Stone  (8) Aerial  (9) Yacht  (10) Fruits  (11) Barbara  (12) Stoke
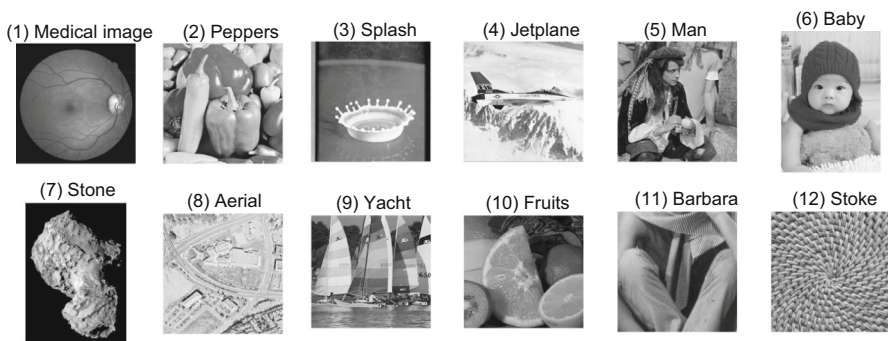
**Fig. 1** All the tested images for noise removal

**Fig. 2** The PSNR values versus $\alpha$ for all the test images with noise removal for noise level $\sigma = 15$. The PSNR values at $\alpha = 1$ correspond to the PSNR values of TV regularization model

**Fig. 3** The PSNR values versus $\alpha$ for all the test images with noise removal for noise level $\sigma = 20$. The PSNR values at $\alpha = 1$ correspond to the PSNR values of TV regularization model

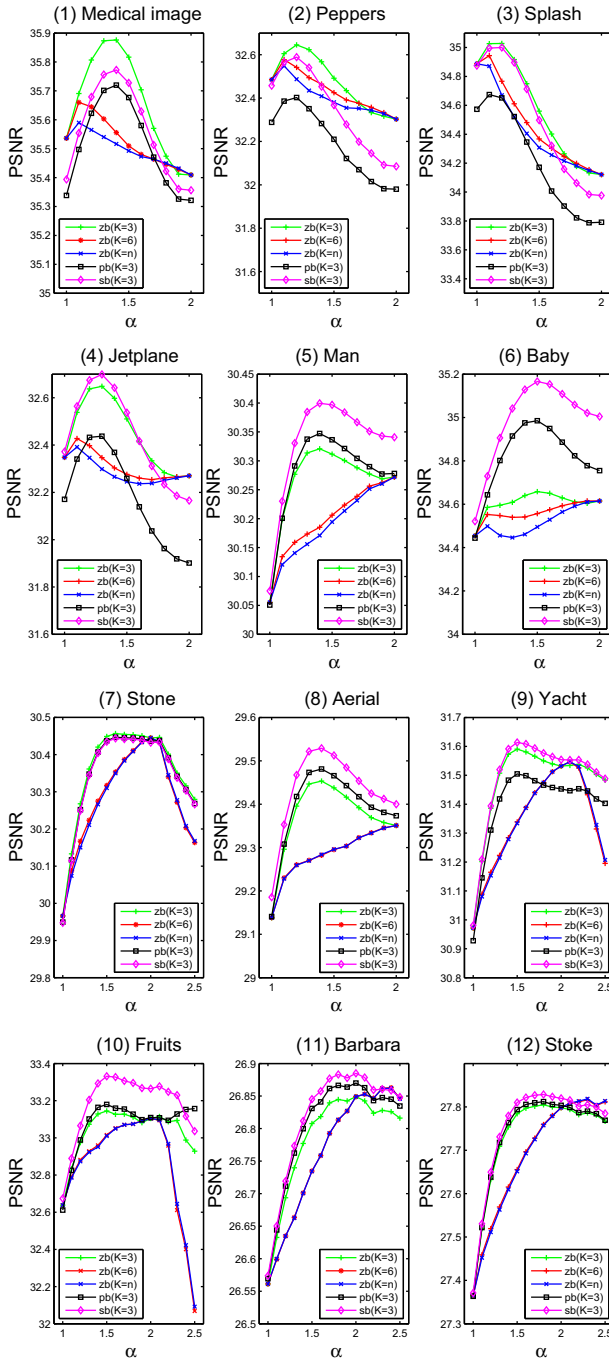**Fig. 4** The figure shows the PSNR values versus $\alpha$ for all the test images with noise removal for noise level $\sigma = 25$. The PSNR values at $\alpha = 1$ correspond to the PSNR values of TV regularization model
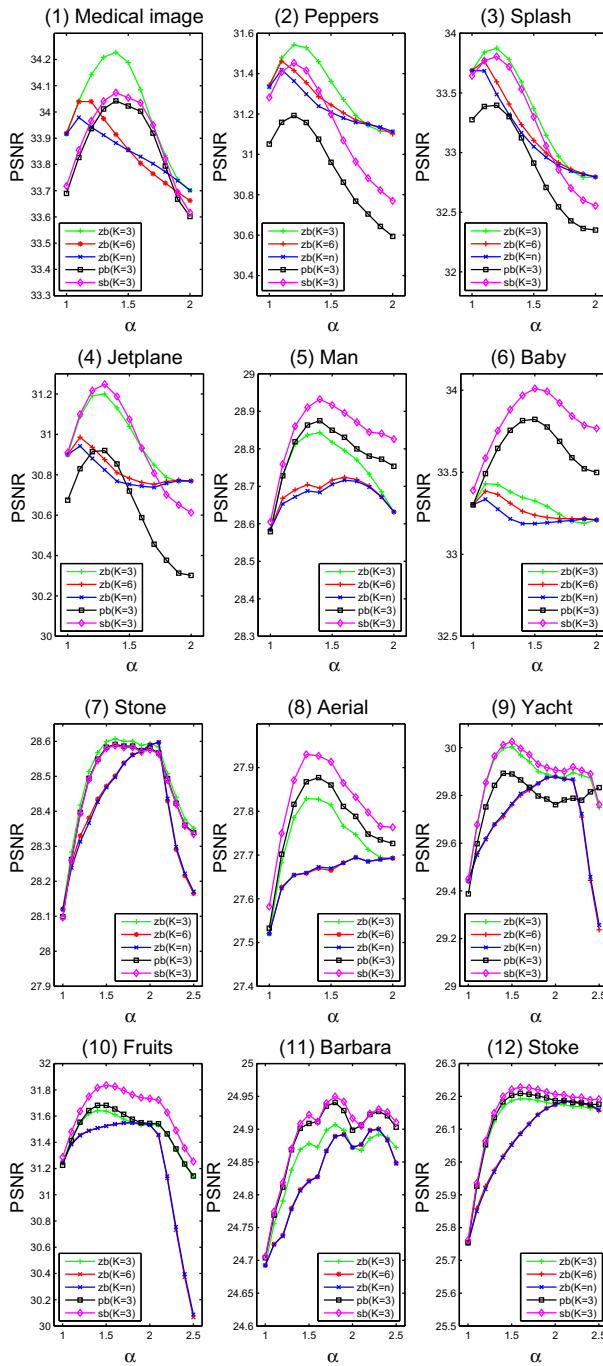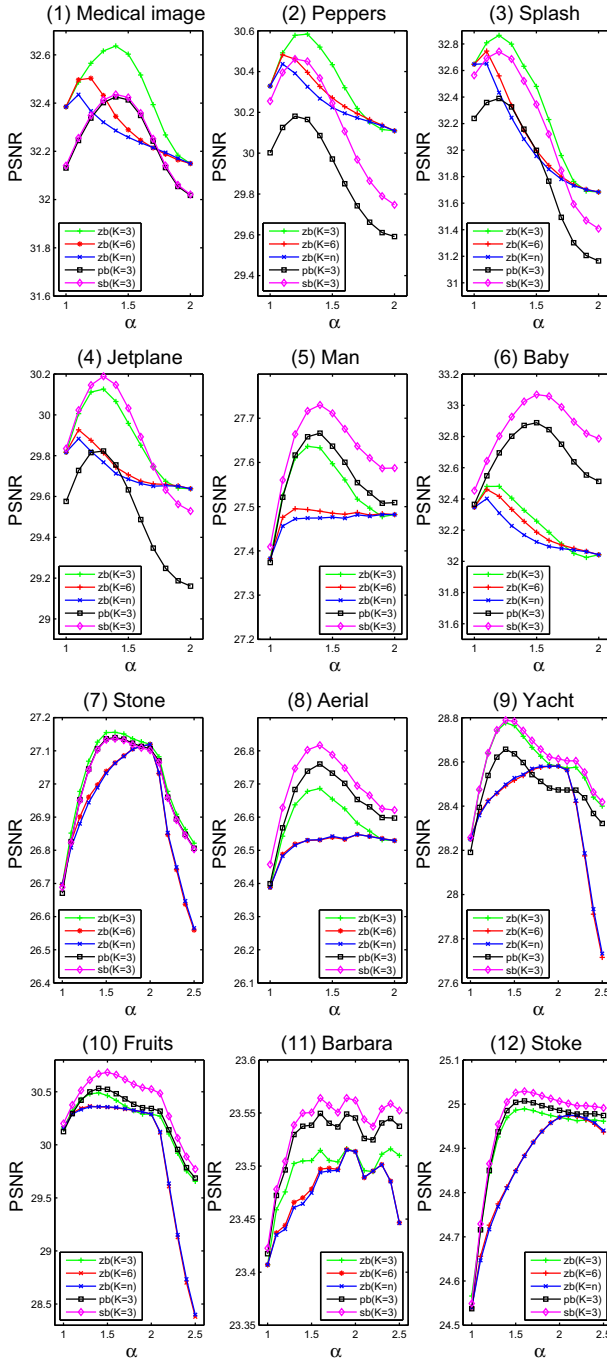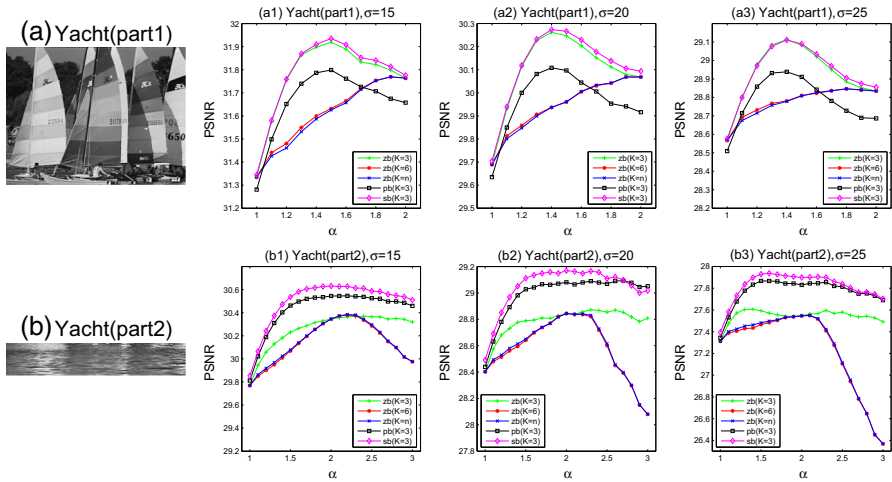
**Fig. 5** Yacht image is divided into two subimages: cartoon image Yacht (part1) and texture image Yacht (part2). Subfigure (a1) to (a3) show the PSNR versus $\alpha$ in the noise removal experiments on Yacht (part1) for different noise levels $\sigma$ =15, 20, 25. Subfigure (b1) to (b3) show the PSNR versus $\alpha$ in the noise removal experiments on Yacht (part1) for different noise levels $\sigma$ =15, 20, 25

to (b3), we are secondly convinced that the fractional order $\alpha$ can be fixed close to 1 for the images having little texture and $\alpha$ can be fixed close to 2 for the images having a lot texture.

## 5.2 Numerical Results on Deblurring

In this section, we discuss the performance of the tFoTV model on deblurring. We compare the proposed tFoTV model with the TV model and the TGV model. The code for the ADMM algorithm to solve the TGV model is adapted from that proposed in [34]. The readers can consult [34] for more details. From the development process, the tFoTV model has similarly simple complexity compared to the TV model, while the TGV model is a little more complex. For both TV and tFoTV models, we need to introduce one multiplier, while we should introduce two multipliers for TGV model. In this paper, we focus on comparing the final results of the three models with sufficient convergence but not the computational cost. For TV model and tFoTV model, we take the tolerance to be $||u^k - u^{k-1}||_2/||u^k||_2 < 10^{-5}$ such that the PSNR of the iterators is almost unchanged. For the TGV model, we fix the maximum of the iteration number to be 500.

We do the numerical experiments on all the images shown in Figs. 1 and 5. Without loss of generalities, all the numerical experiments are finished under the periodic boundary condition. The point spread function generated by the MATLAB command H = fspecial('gaussian', 5, 7) is used to produce the blurred images, and then, the white Gaussian noise of level 10 is added. Following the discussion in Section 5.1, we fix $K = 3$ in tFoTV model and take the fractional orders suggested in Table 1 for the examples shown in Fig. 1. From Fig. 5, we can fix $\alpha = 1.2$ for Yacht (part1) and $\alpha = 1.8$ for Yacht (part2).

**Table 1** The PSNRs of the reconstructed images by TV, the original FoTV model and the tFoTV model on noise removal

| Example | Noisy | | TV | FoTV(ZB) | | tFoTV | | | | BC |
|---|---|---|---|---|---|---|---|---|---|---|
| | $\sigma$ | PSNR | PSNR | $\alpha^\star$ | PSNR | $\alpha^\star$ | PSNR | $\alpha$ | PSNR | |
| (1) Medical Im. | 15 | 25.21 | 35.54 | 1.1 | 35.59 | 1.4 | **35.88** | 1.2 | 35.81 | ZB |
| | 20 | 22.76 | 33.92 | l.1 | 33.97 | 1.4 | **34.23** | 1.2 | 34.14 | ZB |
| | 25 | 20.88 | 32.38 | 1.1 | 32.44 | 1.4 | **32.64** | 1.2 | 32.57 | ZB |
| (2) Peppers | 15 | 24.68 | 32.48 | 1.1 | 32.55 | 1.2 | 32.65 | 1.2 | **32.65** | ZB |
| | 20 | 22.21 | 31.28 | 1.1 | 31.42 | 1.2 | 31.45 | 1.2 | **31.45** | ZB |
| | 25 | 20.32 | 30.33 | 1.1 | 30.44 | 1.2 | 30.58 | 1.2 | **30.58** | ZB |
| (3) Splash | 15 | 24.68 | 34.89 | 1.0 | 34.89 | 1.2 | 35.03 | 1.2 | **35.03** | ZB |
| | 20 | 22.27 | 33.64 | 1.1 | 33.68 | 1.2 | 33.80 | 1.2 | **33.80** | ZB |
| | 25 | 20.37 | 32.65 | 1.1 | 32.65 | 1.2 | 32.87 | 1.2 | **32.87** | ZB |
| (4) Jetplane | 15 | 24.62 | 32.37 | 1.1 | 32.39 | 1.2 | 32.67 | 1.2 | **32.67** | SB |
| | 20 | 22.17 | 30.91 | 1.1 | 30.94 | 1.3 | **31.25** | 1.2 | 31.22 | SB |
| | 25 | 20.36 | 29.83 | 1.1 | 29.88 | 1.3 | **30.19** | 1.2 | 30.15 | SB |
| (5) Man | 15 | 24.97 | 30.08 | 2.0 | 30.27 | 1.4 | **30.40** | 1.2 | 30.33 | SB |
| | 20 | 22.54 | 28.60 | 1.6 | 28.72 | 1.4 | **28.93** | 1.2 | 28.86 | SB |
| | 25 | 20.65 | 27.41 | 2.0 | 27.48 | 1.4 | **27.73** | 1.2 | 27.66 | SB |
| (6) Baby | 15 | 24.63 | 34.52 | 2.0 | 34.61 | 1.5 | 35.17 | 1.5 | **35.17** | SB |
| | 20 | 22.16 | 33.39 | 1.1 | 33.34 | 1.5 | 34.01 | 1.5 | **34.01** | SB |
| | 25 | 20.27 | 32.45 | 1.1 | 32.40 | 1.5 | 33.07 | 1.5 | **33.07** | SB |
| (7) Stone | 15 | 25.97 | 29.97 | 2.0 | 30.44 | 1.6 | **30.46** | 1.5 | 30.45 | ZB |
| | 20 | 23.50 | 28.12 | 2.1 | 28.60 | 1.6 | **28.61** | 1.5 | 28.60 | ZB |
| | 25 | 21.59 | 26.70 | 2.0 | 27.12 | 1.5 | 27.16 | 1.5 | **27.16** | ZB |
| (8) Aerial | 15 | 24.65 | 29.19 | 2.0 | 29.35 | 1.4 | **29.53** | 1.5 | 29.50 | SB |
| | 20 | 22.20 | 27.58 | 1.7 | 27.69 | 1.3 | **27.93** | 1.5 | 27.91 | SB |
| | 25 | 20.34 | 26.46 | 1.7 | 26.55 | 1.4 | **26.82** | 1.5 | 26.79 | SB |
| (9) Yacht | 15 | 24.69 | 30.98 | 2.0 | 31.55 | 1.5 | 31.61 | 1.5 | **31.61** | SB |
| | 20 | 22.22 | 29.45 | 2.0 | 29.88 | 1.5 | 30.03 | 1.5 | **30.03** | SB |
| | 25 | 20.34 | 28.26 | 2.0 | 28.58 | 1.4 | **28.79** | 1.5 | 28.78 | SB |
| (10) Fruits | 15 | 24.77 | 32.66 | 2.0 | 33.10 | 1.5 | 33.33 | 1.5 | **33.33** | SB |
| | 20 | 22.36 | 31.25 | 1.7 | 31.55 | 1.5 | 31.84 | 1.5 | **31.84** | SB |
| | 25 | 20.47 | 30.20 | 1.4 | 30.36 | 1.5 | 30.68 | 1.5 | **30.68** | SB |
| (11) Barbara | 15 | 24.71 | 26.57 | 2.4 | 26.87 | 1.8 | 26.88 | 1.8 | 26.88 | SB |
| | 20 | 22.26 | 24.71 | 2.3 | 24.90 | 1.8 | **24.95** | 1.8 | **24.95** | SB |
| | 25 | 20.43 | 23.42 | 1.9 | 23.52 | 1.6 | **23.56** | 1.8 | 23.55 | SB |

**Table 1** continued

| Example | Noisy | | TV | FoTV(ZB) | | tFoTV | | | | BC |
|---|---|---|---|---|---|---|---|---|---|---|
| | $\sigma$ | PSNR | PSNR | $\alpha^\star$ | PSNR | $\alpha^\star$ | PSNR | $\alpha$ | PSNR | |
| (12) Stoke | 15 | 24.64 | 27.37 | 2.3 | 27.82 | 1.8 | 27.83 | 1.8 | **27.83** | SB |
| | 20 | 22.15 | 25.76 | 2.2 | 26.19 | 1.6 | **26.23** | 1.8 | 26.22 | SB |
| | 25 | 20.26 | 24.55 | 2.1 | 24.98 | 1.6 | **25.03** | 1.8 | 25.02 | SB |

The numbers in bold are the highest PSNR values. $\alpha^\star$ is the optimal $\alpha$ with which the original FoTV and tFoTV produce the highest PSNR values, respectively. The last column shows the boundary condition under which the highest PSNR values are obtained when the TV model and tFoTV model are implemented. BC, ZB, PB and SB are the abbreviations for boundary condition, Dirichlet homogeneous, periodic and Neumann boundary conditions, respectively

The PSNR values of the recovered images by TV, TGV and tFoTV models are listed in Table 2. The highest PSNR values are marked in red. From the results, we see that the tFoTV model can produce more accurate reconstructions than the TV model and compete the results by the TGV model.

**Table 2** The PSNRs of the reconstructed images by TV, TGV model and the tFoTV models on moving blur

| Example | Blurred&Noisy | TV | TGV | tFoTV | |
|---|---|---|---|---|---|
| | PSNR | PSNR | PSNR | $\alpha$ | PSNR |
| (1) Medical Im. | 27.88 | 35.43 | 35.59 | 1.2 | **35.61** |
| (2) Peppers | 25.21 | 29.58 | **29.94** | 1.2 | 29.75 |
| (3) Splash | 26.29 | 32.84 | 32.85 | 1.2 | **32.98** |
| (4) Jetplane | 24.46 | 28.28 | **28.43** | 1.2 | **28.43** |
| (5) Man | 23.84 | 27.05 | 27.14 | 1.2 | **27.20** |
| Yacht (part1) | 23.33 | 27.43 | 27.46 | 1.2 | **27.62** |
| (6) Baby | 27.16 | 33.54 | **33.98** | 1.5 | 33.92 |
| (7) Stone | 24.56 | 27.09 | **27.64** | 1.5 | 27.62 |
| (8) Aerial | 22.08 | 24.58 | 24.71 | 1.5 | **24.80** |
| (9) Yacht | 23.35 | 27.34 | 27.37 | 1.5 | **27.46** |
| (10) Fruits | 26.18 | 30.53 | **30.76** | 1.5 | 30.72 |
| Yacht (part2) | 23.82 | 26.50 | **27.12** | 1.8 | 26.85 |
| (11) Barbara | 19.91 | 21.04 | **21.22** | 1.8 | 21.14 |
| (12) Stoke | 23.01 | 24.71 | **25.12** | 1.8 | 25.02 |

The numbers in bold are the highest PSNR values. $\alpha$ in tFoTV model is suggested in Sect. 5.1

## 6 Conclusion

In this paper, we propose a modified truncation to generate the fractional-order gradient operator and apply the tFoTV model to image restoration. The alternating directional method is developed to solve the proposed model. After taking the modified truncation, any boundary condition can be used in the numerical experiments and the accuracy of the recovered images is improved. The brief convergence analysis of the ADMM for the tFoTV model can also be developed. We apply the proposed tFoTV model to noise removal and deblurring. The numerical results show that the tFoTV model produces more accurate reconstructions in PSNR than TV model and is comparable with the TGV model. As mentioned in the paper, in the tFoTV model, the fractional order can be roughly fixed from the structure of the observed images, and therefore, there is only one regularization parameter left to determine, while in the TGV model, there are always two regularization parameters to be fixed in the numerical experiments.

## References

[1] Rudin, L.I., Osher, S., Fatemi, E.: Nonlinear total variation based noise removal algorithms. Physica D **60**, 259–268 (1992)
[2] Lysaker, M., Lundervold, A., Tai, X.-C.: Noise removal using fourth-order partial differential equation with applications to medical magnetic resonance images in space and time. IEEE Trans. Imaging Process. **12**, 1579–1590 (2003)
[3] Chan, R.H., Liang, H., Wei, S., Nikolova, M., Tai, X.-C.: High-order total variation regularization approach for axially symmetric object tomography from a single radiograph. Inverse Probl. Imaging **9**, 55–77 (2015)
[4] Lysaker, M., Tai, X.-C.: Iterative image restoration combining total variation minimization and a second-order functional. Int. J. Comput. Vis. **66**, 5–18 (2005)
[5] Bredies, K., Kunisch, K., Pock, T.: Total generalized variation. SIAM J. Imaging Sci. **3**, 492–526 (2010)
[6] Knoll, F., Bredies, K., Pock, T., Stollberger, R.: Second order total generalized variation (TGV) for MRI. Magn. Reson. Med. **65**, 480–491 (2011)
[7] Lavoie, J.L., Osler, T.J., Tremblay, R.: Fractional derivatives and special functions. SIAM Rev. **18**, 240–268 (1976)
[8] Podlubny, I.: Fractional Differential Equations. Academic Press, New York (1999)
[9] Podlubny, I., Chechkin, A., Skovranek, T., Chen, Y., Jara, B.M.V.: Matrix approach to discrete fractional calculus II: partial fractional differential equations. J. Comput. Phys. **228**(8), 3137–3153 (2009)
[10] Mathieu, B., Melchior, P., Oustaloup, A., Ceyral, C.: Fractional differentiation for edge detection. Signal Process. **83**, 2421–2432 (2002)
[11] Bai, J., Feng, X.C.: Fractional-order anisotropic diffusion for image denoising. IEEE Trans. Image Process. **16**(10), 2492–2502 (2007)
[12] Chan, R.H., Lanza, A., Morigi, S., Sgallari, F.: An adaptive strategy for restoration of textured images using fractional order regularization. Numer. Math. Theory Methods Appl. **6**, 276–296 (2013)
[13] Cuesta, E., Kirane, M., Malik, S.: Image structure preserving denoising using genelized fractional time integrals. Signal Process. **92**, 553–563 (2012)
[14] Hu, X., Li, Y.: A new variational model for image denoising based in fractional-order derivative. In: 2012 International Conference on Systems and Informatics (ICSAI), pp. 1820–1824 (2012)
[15] Larnier, S., Mecca, R.: Fractional-order diffusion for image reconstruction. In: 2012 IEEE International Conference on Acoustics, Speech and Signal Processing, pp. 1057–1060 (2012)
[16] Pu, Y., Zhou, J., Siarry, P., Zhang, N., Liu, Y.: Fractional partial differential equation: fractional total variation and fractional steepest decent approach-based multiscale denoising model for texture image. Abstr Appl Anal. (2013). https://doi.org/10.1155/2013/483791

[17] Xu, J., Feng, X., Hao, Y.: A coupled variational model for image denoising using a duality strategy and split Bregman. Multidimens. Syst. Signal Process. **25**, 83–94 (2014)

[18] Zhang, J., Chen, K.: A Total fractional-order variation model for image restoration with non-homogeneous boundary conditions and its numerical solution, Computer Vision and Pattern Recognition (2015). arXiv:1509.04237.pdf

[19] Zhang, J., Wei, Z., Xiao, L.: Adaptive fractional-order multi-scale method for image denoising. J. Math. Imaging Vis. **43**, 39–49 (2011)

[20] Zhang, J., Wei, Z.: A class of fractional-order multi-scale variational models and alternating projection algorithm for image denoising. Appl. Math. Model. **35**(5), 2516–2528 (2011)

[21] Wang, W., Lu, P.: A new image deblurring method based on fractional differential. In: Audio, Language and Image Processing, pp. 497–501 (2012)

[22] Tian, D., Xue, D., Chen, D., Sun, S.: A fractional-order regulatory CV model for brain MR image segmentation. In: 2013 Chinese Control and Decision Conference, pp. 37–40 (2013)

[23] Zhang, Y., Pu, Y.-F., Hu, J.-R., Zhou, J.-L.: A class of fractional-order variational image inpainting models. Appl. Math. Inf. Sci. **6**(2), 299–306 (2012)

[24] Zhang, J., Wei, Z.: Fractional variational model and algorithm for image denoising. In: Proceedings of the Fourth International Conference on Natural Computation., vol 5, pp. 524–528. IEEE, Washington (2008)

[25] Glowinski, R., Marrocco, A.: Sur L'approximation, par elements finis d'ordre un, et la resolution, par penalisationdualite, dune classe de problems de Direchlet non linaries. R. A. I. O. R2 **9**(R–2), 41–76 (1975)

[26] Gabay, D., Mercier, B.: A dual algorithm for the solution of nonlinear variational problems via finite element approximation. Comput. Math. Appl. **2**(1), 17–40 (1976)

[27] Wu, C.L., Tai, X.C.: Augmented Lagrangian method, dual methods, and split Bregman iteration for ROF, vectorial TV, and high order models. SIAM J. Imaging Sci. **3**, 300–339 (2010)

[28] Wu, C.L., Zhang, J.Y., Tai, X.C.: Augmented Lagrangian method for total variation restoration with non-quadratic fidelity. Inverse Probl. Imaging **5**, 237–261 (2010)

[29] Tai, X.C., Wu, C.L.: Augmented Lagrangian method, dual methods and split Bregman iteration for ROF model. In: Scale Space and Variational Methods in Computer Vision, Second International Conference, SSVM 2009, Voss, Norway, June 1–5, 2009. Proceedings. Lecture Notes in Computer Science 5567, pp. 502–513. Springer, Heidelberg (2009)

[30] Zhang, X., Burger, M., Osher, S.: A unified primal-dual algorithm framework based on Bregman iteration. J. Sci. Comput. **46**(1), 20–46 (2011)

[31] Goldstein, T., Osher, S.: The split Bregman method for l1-regularized problems. SIAM J. Imaging Sci. **2**, 323–343 (2009)

[32] Deng, W., Yin, W.: On the global and linear convergence of generalized alternating direction method of multipliers. J. Sci. Comput. **66**(3), 889–916 (2016)

[33] Eckstein, J., Bertsekas, D.: On the Douglas-Rackford Splitting Method and Proximal Point Algorithm for Maximal Monotone Operators, Mathematical Programming, vol. 55. North-Holland, Amsterdam (1992)

[34] Guo, W., Qin, J., Yin, W.: A new detail-preserving regularity scheme. SIAM J. Imaging Sci. **7**(2), 1309–1334 (2014)